Supporting Information S1 for "Saturn's innermost radiation belt throughout and inward of the D-ring"

P. Kollmann[1], E. Roussos[2], A. Kotova[3], L. Regoli[4], D. G. Mitchell[1], J. Carbary[1], G. Clark[1], N. Krupp[2], C. Paranicas[1]

[1]Johns Hopkins University Applied Physics Laboratory, Laurel, MD 20723-6099, USA
[2]Max Planck Institute for Solar System Research, 37077 Göttingen, Germany
[3]IRAP, University de Toulouse, CNRS, UPS, CNES, Toulouse, France
[4]Department of Climate and Space Sciences and Engineering, University of Michigan, Ann Arbor, MI 48109-2143, USA

Contents

Text

Figures

Corresponding author: Peter Kollmann, Peter.Kollmann@jhuapl.edu

S .1.1 Raw Data

Our analysis is based on data from the LEMMS instrument (low energy magnetospheric measurement system), part of the MIMI suite [*Krimigis et al.*, 2004; *Krupp et al.*, 2009; *Vandegriff et al.*, 2013; *Roussos and Kollmann et al.*, 2018; *Roussos et al.*, 2018a]. As in *Roussos and Kollmann et al.* [2018], we base our analysis on instrument channels referred to as P8 and E7 that measure protons > 25MeV and > 300MeV, respectively. These channels use LEMMS' main stack of solid state detectors.

LEMMS is only sampling one pitch angle (angle between particle velocity and magnetic field) at a time. Generally, this limitation can be mitigated when Cassini is spinning, but the occasional spins while passing the innermost radiation belt were not fast enough to achieve good coverage. We therefore statistically build up pitch angle distributions over the 23 available orbits. This approach is justified since the proton distribution appears extremely stable in time, at least over the 6 months when it was observed. The statistical approach works well for distances of $L > 1.05$, but data are too sparse inward of this distance. We therefore do not consider smaller distances here, even though there are LEMMS channels with significant counts down to $L \approx 1.03$, where the atmospheric density strongly increases. The two used channels are not dominated by contamination and no significant counts over the A-C-rings ($L > 1.24$). These rings are an $\approx 1R_S$ wide particle-absorbing region that permanently separates the innermost radiation belt from the previously known outer radiation belts ($2.27 < L < 4.9$), in a similar way as the outer belts are segregated by the moons.

We organize the data as a function of L-shell (respective field line's distance from Saturn's rotation axis at the magnetic equator), equatorial pitch angle, and effective latitude. All these quantities rely on a third-order multipole model for Saturn's internal magnetic field [*Roussos et al.*, 2018b] that has similar parameters as *Cao et al.* [2011]. The effective latitude is the latitude in a dipole field that has the same L-shell and ratio between local and equatorial magnetic field as our third-order multipole model. We use this kind of latitude because it allows us to conveniently convert between local and equatorial pitch angle through the analytic expressions for a dipole field, while still allowing to use quantities traced in a more realistic field model. Raw data organized by these quantities can be found in Figs. S .1.5, S .1.6, and S .1.9. It can be seen that there is a latitude dependence in count rates that are measured at the same L-shell and equatorial pitch angle. This dependence is robust and also shows for other latitude definitions.

A latitude dependence of the count rates indicates that the instrument is counting particles that penetrate its shielding instead of only counting particles that enter through its nominal aperture. Since the penetrators are trapped at the equatorial plane, this leads to the observed latitude dependence [*Roussos and Kollmann et al.*, 2018].

S .1.2 Forward Model

The penetrators found in Sec. S .1.1 imply that LEMMS' standard calibration cannot be used. Instead, we use a new calibration that can account for penetrators [*Roussos and Kollmann et al.*, 2018; *Roussos et al.*, 2018a] and forward modeling to convert the raw count rates into intensities. We assume that the differential intensities (particles per time, area, solid angle, energy interval) follow some function $j(E, \alpha_{eq})$ that depends on kinetic energy E and equatorial pitch angle α_{eq}. A possible function is for example given in Eq. (1). The modeled count rate R_r is then

$$R_r = \int_0^{\pi} \mathrm{d}\theta \int_0^{2\pi} \mathrm{d}\varphi \int_0^{\infty} \mathrm{d}E \; j(E, \alpha_{eq}) \; g_d(E, \theta, \varphi) \; \sin(\theta) \tag{15}$$

g_d is the differential geometry factor describing the instrument response. θ and φ describe the particle's velocity direction relative to the instrument in spherical coordinates and are related to the pitch angle α_{eq} via the spherical law of cosines (see for example *Li et al.* [2013]).

Note that Eq. (15) reproduces the combined count rate of contamination and foreground. The modeled count rate R_r can therefore directly be compared with the measured count rate R_m without any background subtraction.

Since running the forward model is computationally expensive, we do not calculate R_r for every single measurement with 3s time resolution but instead average the count rates from all orbits into bins in L-shell, equatorial pitch angle, and effective latitude. In Figs. S .1.6 to S .1.10 we show the binning procedure and compare binned with modeled count rates for the models and locations shown in Fig. 1 of the main paper. It can be seen that the value of Δ is a good indication of the fit quality. We check for outliers from this behavior after each model run. Only results are considered as good if $\Delta \leq 0.1$ and $\delta_i < 1$ for all i measurements.

S .1.3 Relation between PADs and neutral densities

In this section we derive Eq. (5), the quantitative relation between the atmospheric density $n(\vec{r})$ and the PAD $j(\alpha_{eq})$. Here, $\vec{r}$ is the location of the particle that we describe as altitude relative to the 1-bar surface. We use altitude instead of radial distance to account for Saturn's oblate shape.

How neutral densities affect proton intensities j can be calculated by considering the proton phase space density f in momentum (p) space, which is related to the intensity j [*Walt*, 1994] by

$$f(E, \alpha_{eq}) = \frac{j(E, \alpha_{eq})}{p(E)^2} \tag{16}$$

If we assume that a radiation belt is in steady state, supplied by a source S, and depleted by losses $\mathrm{d}f/\mathrm{d}t$, its phase space density can be calculated by solving

$$S = \sum_k^K \left.\frac{\mathrm{d}f}{\mathrm{d}t}\right|_k \tag{17}$$

with

$$\left.\frac{\mathrm{d}f}{\mathrm{d}t}\right|_k = \frac{v}{p^2}\frac{\partial}{\partial E}\left(j\,\frac{\widetilde{n}_k}{n_{0,k}}\left.\frac{\mathrm{d}E}{\mathrm{d}x}\right|_k\right) \tag{18}$$

The index k runs over the K neutral targets considered, for example atmospheric H_2 and H_2O from rings.

Equation (18) describes the particle loss through energy loss (*Schulz and Lanzerotti* [1974]; *Kollmann et al.* [2013], appendix A2). Energy loss of a proton in neutral material is described through $(\mathrm{d}E/\mathrm{d}x)(\widetilde{n}/n_0)$. $\mathrm{d}E/\mathrm{d}x$ represents tabulated values [*Berger et al.*, 2005] of the energy loss per distance in a medium of density n_0, usually with a value as it exists under standard conditions on Earth. $\widetilde{n}$ is the average density that the actual medium in space has.

The source S is mostly depending on energy. Its energy dependence can be determined through CRAND simulations [*Blake et al.*, 1983; *Cooper et al.*, 2018]. Its radial dependence follows $S \propto L^m$ with $m \leq 3$ [*Kollmann et al.*, 2015]. This means that we expect S to change by less than a factor of 2 over the L-range considered here. Since this is less than the 2-3 order of magnitude intensity change we observe (Fig. 2), we consider S as L-independent. The pitch angle dependence of S is much weaker than the observed pitch angle dependence of j (*Roussos and Kollmann et al.* [2018]). We therefore assume that S is also independent on pitch angle.

Equations (17) and (18) can be immediately solved for $J(\alpha_{eq})$ if the PAD is energy-independent (Eq. 1) and in case of a single dominating target material ($K = 1$).

$$J = \frac{S\,p^2}{j_A\;v\;\frac{\mathrm{d}}{\mathrm{d}E}\left(\mathcal{A}\,\mathrm{d}E/\mathrm{d}x\right)}\frac{n_0}{\widetilde{n}} = \frac{n_A}{\widetilde{n}} \tag{19}$$

which is identical to Eq. (5) provided in Sec. 3.2. The expression on the right hand side defines n_A, one of the free parameter in our forward model (Sec 3.2). While the expression on the right hand side is independent on energy, the expression in the middle of Eq. (19) is formally energy dependent. This apparent discrepancy resolves if our assumptions are approximately true: Since the spectrum $\mathcal{A}$ is shaped by the balance of energy loss $\mathrm{d}E/\mathrm{d}x$ and source S, it will take a form that cancels out the energy dependence of the other terms.

Equation (18) is most applicable for the energy range considered here, namely for MeV to hundreds of MeV. At lower energies, terms for charge exchange [*Lindsay and Stebbings*, 2005] and neutralization [*Mauk et al.*, 1998] would need to be added. At higher energies, inelastic nuclear collisions [*Janni*, 1982] would need to be considered. All of these processes scale with the neutral material density in the same way as energy loss, so that their inclusion does not change the proportionality on the right hand side of Eq. (19).

S .1.4 Relating ring and exosphere densities

We argue in Sec. 5 that there is a location L_p where

$$\left.\frac{\mathrm{d}f}{\mathrm{d}t}\right|_{\mathrm{rng}} = \left.\frac{\mathrm{d}f}{\mathrm{d}t}\right|_{\mathrm{exo}} \tag{20}$$

Equation (20) can be reformed with Eqs. (18) and (1)

$$\frac{\frac{\partial}{\partial E}\left(\frac{\mathcal{A}(E)}{n_{0,\mathrm{rng}}}\left.\frac{\mathrm{d}E}{\mathrm{d}x}\right|_{\mathrm{rng}}\right)}{\frac{\partial}{\partial E}\left(\frac{\mathcal{A}(E)}{n_{0,\mathrm{exo}}}\left.\frac{\mathrm{d}E}{\mathrm{d}x}\right|_{\mathrm{exo}}\right)} = \frac{\widetilde{n}_{\mathrm{exo}}}{\widetilde{n}_{\mathrm{rng}}} \approx 0.2 \tag{21}$$

The factor 0.2 is determined by evaluating the left hand side of the equation. The required inputs are $\mathcal{A}(E) \propto j$ from our forward models and tabulated values of $\mathrm{d}E/\mathrm{d}x/n_0$ for the H_2 exosphere and the H_2O ring that we take from *Berger et al.* [2005]. Even though the left side is generally energy dependent it turns out that its strongest dependence is for < 1MeV, while its values throughout our energy range (> 25MeV) are limited in the narrow range of 0.22 to 0.25. This factor provides the relation between ring and exosphere densities at L_p that was already provided in Eq. (10).

Note that Eq. (21) does not depend on the absolute proton intensity nor makes strong assumptions on the source process S, which makes this method of determining the D-ring density from radiation data relatively robust.

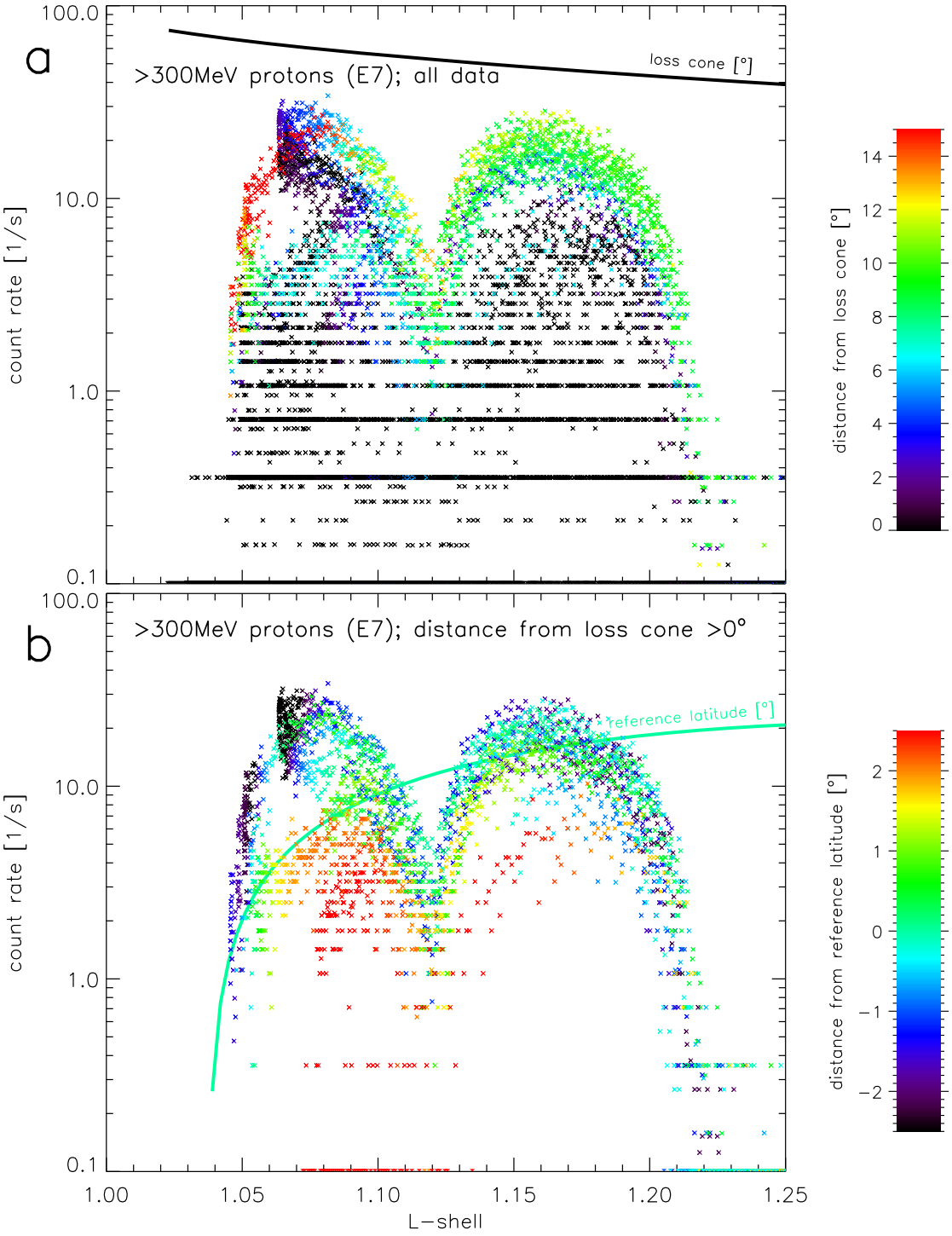

Figure S .1.5. Raw count rates of > 300MeV protons in Saturn's innermost radiation belt as a function of L-shell. Panel A: x-symbols show count rates, their color represents the instrument look direction, expressed as equatorial pitch angle minus equatorial loss cone angle. The loss cone angle is shown by the black curve. It can be seen that the lowest intensities are usually found in the loss cone, indicating that this channel measures protons through the instrument aperture, as it was designed to do. Most other LEMMS channels (not shown) have very similar count rates both in and outside the loss cone, indicating that they are dominantly counting penetrators. Panel B: Axes are as in panel A but only data points outward of the loss cone are shown. Color represents now Cassini's location relative to a reference latitude. This latitude is a smooth version of the average latitude covered during Cassini's various orbits and is shown as a green curve. It can be seen that the count rates increase with decreasing latitude. Closer inspection (for example Fig. S .1.6 and S .1.9) shows that the latitude dependence is independent of the pitch angle dependence. This indicates that even the shown channel counts some particles that penetrate the instrument and are most abundant at low latitudes.

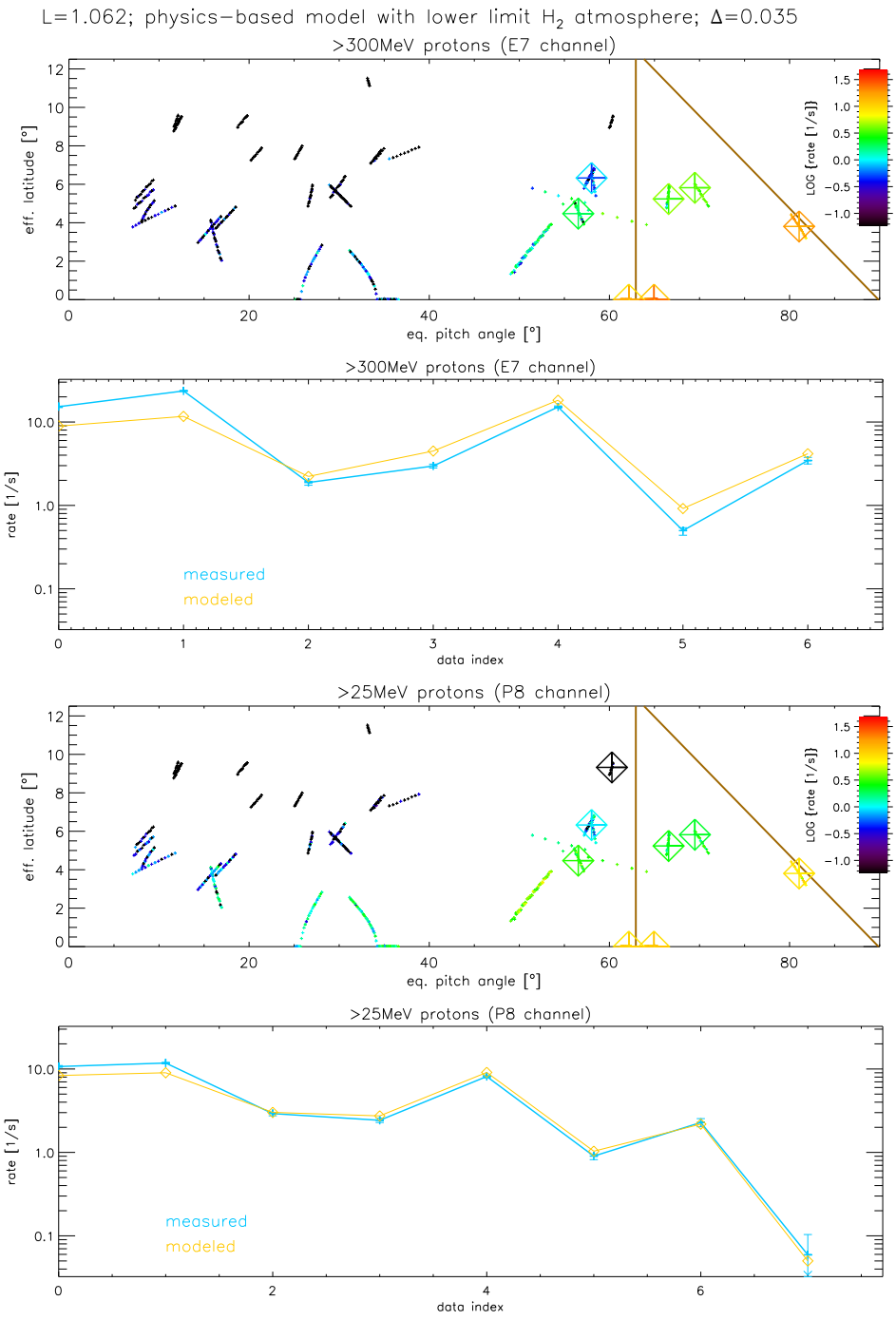

Figure S .1.6. Comparison between modeled and measured count rates. This figure shows data from $L = 1.062$ using the model based on the "lower limit" atmosphere, see the blue curve in Fig. 1a. The upper two and lower two panels show count rates from the E7 and P8 channels of LEMMS, respectively. For each channel we show the rates in two ways. The upper panel for each channel shows the equatorial pitch angle and effective latitude of the measurement. Count rate values are color coded. Small "+"-symbols represent the single measurements, large "+"-symbols show the binned count rates, large diamonds the modeled count rates. The vertical brown line shows the geometric loss cone location. Only particles with equatorial pitch angles below the diagonal brown line are able to reach the given latitudes, other pitch angles mirror below the spacecraft. The lower panels of each channel show count rates on the y-axis, which is more quantitative than the color coding in the upper panels. Error bars show the Poisson error of the measurements but are often smaller than the "+"-symbols of the data points. The x-axis shows a running index that mixes pitch angle and latitude dependence. Lines between the points are only to guide the eye. The RMS-log-error between measurement and model is provided by the Δ-value in the title of the figure.

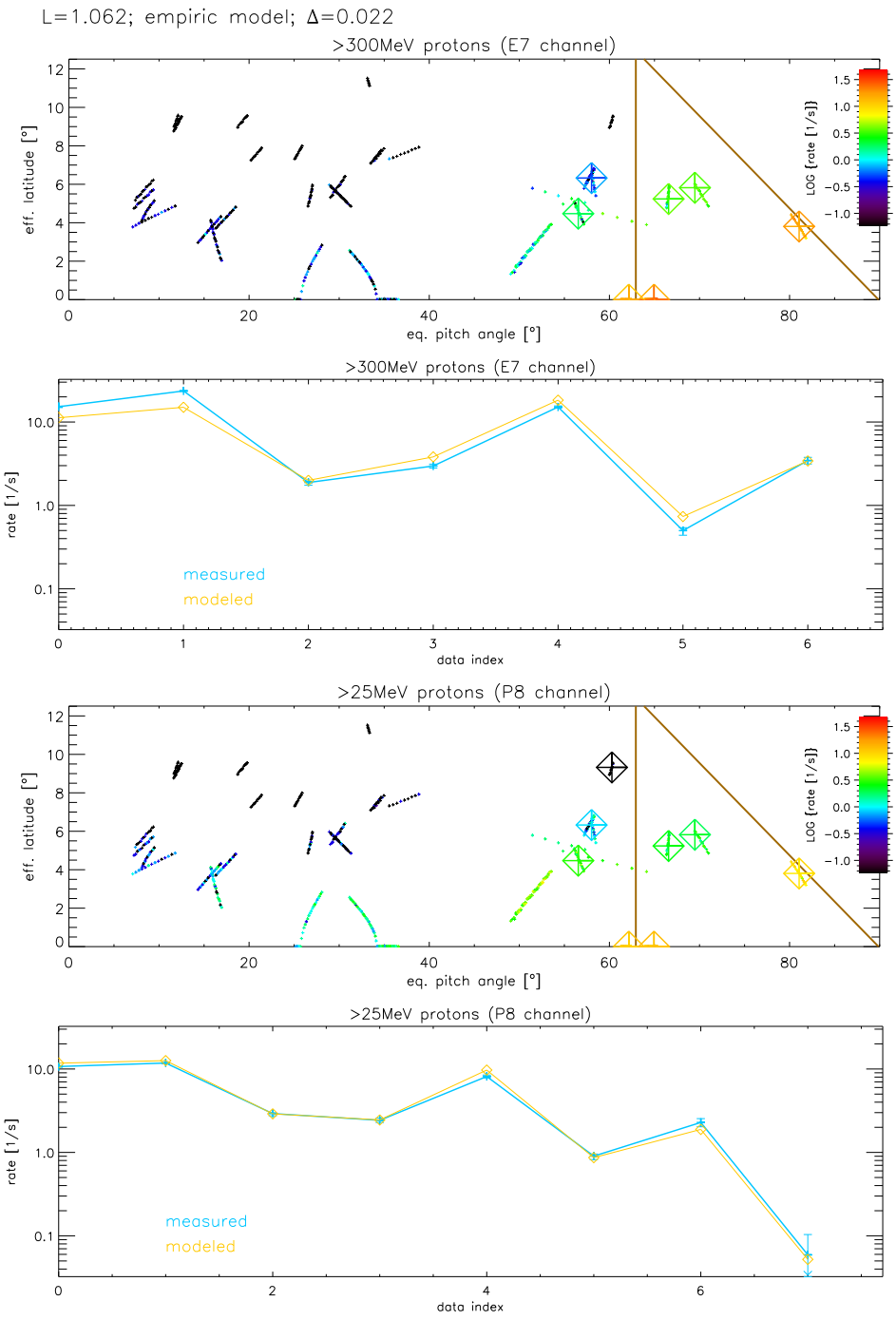

Figure S .1.7. Comparison between modeled and measured count rates. This figure shows data from $L = 1.062$ using the empiric PAD model, see the green curve in Fig. 1a. Otherwise like Fig. S .1.6.

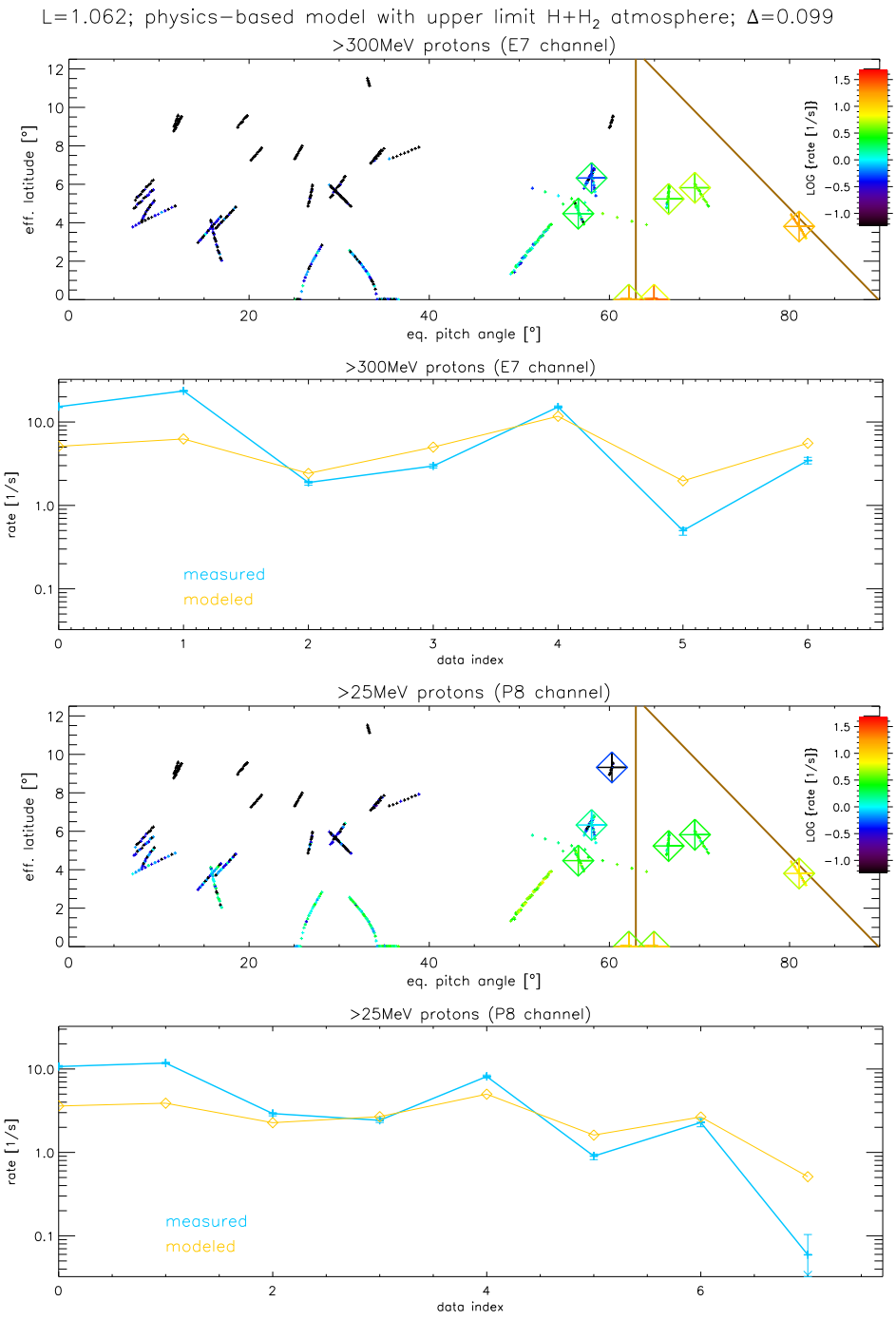

Figure S .1.8. Comparison between modeled and measured count rates. This figure shows data from $L = 1.062$ using the model based on the "upper limit" atmosphere, see the red curve in Fig. 1a. The fit here is worse than in Fig. S .1.6 and S .1.7, which is captured by the larger error Δ. Otherwise like Fig. S .1.6.

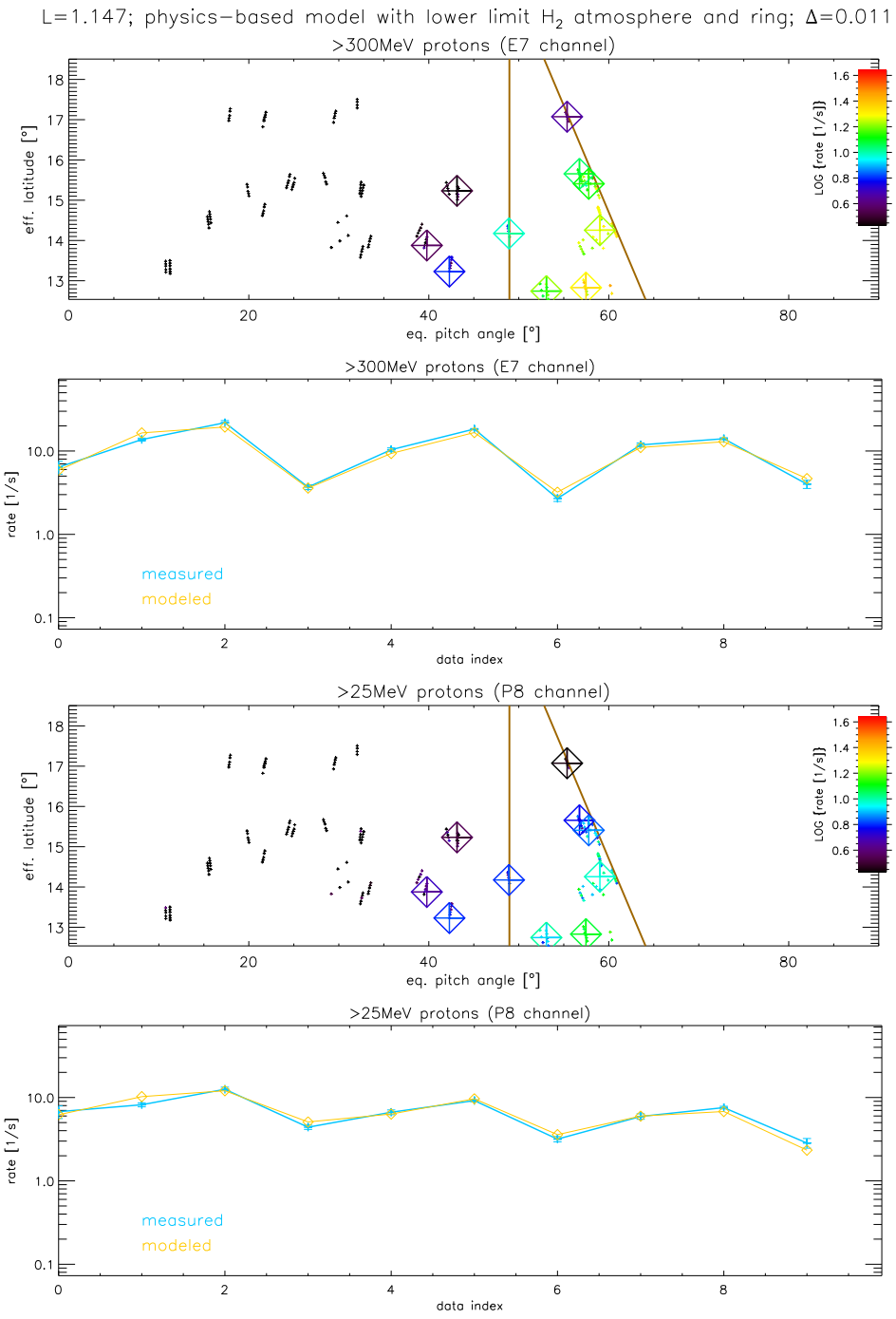

Figure S .1.9. Comparison between modeled and measured count rates. This figure shows data from $L = 1.147$ using the model based on the "lower limit" atmosphere plus D-ring, see the black curve in Fig. 1b. Otherwise like Fig. S .1.6.

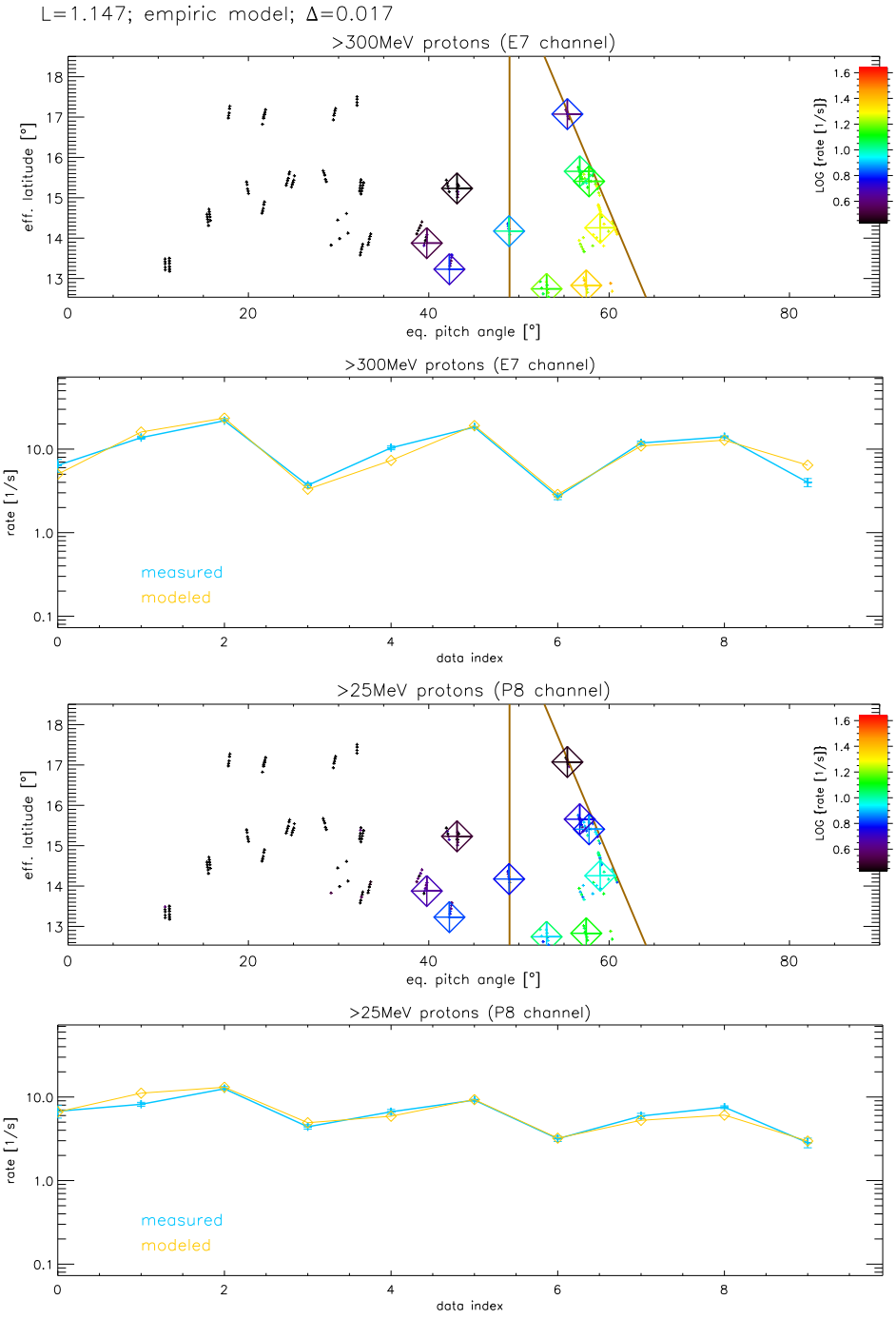

Figure S .1.10. Comparison between modeled and measured count rates. This figure shows data from $L = 1.147$ using the empiric PAD model, see the green curve in Fig. 1b. Otherwise like Fig. S .1.6.

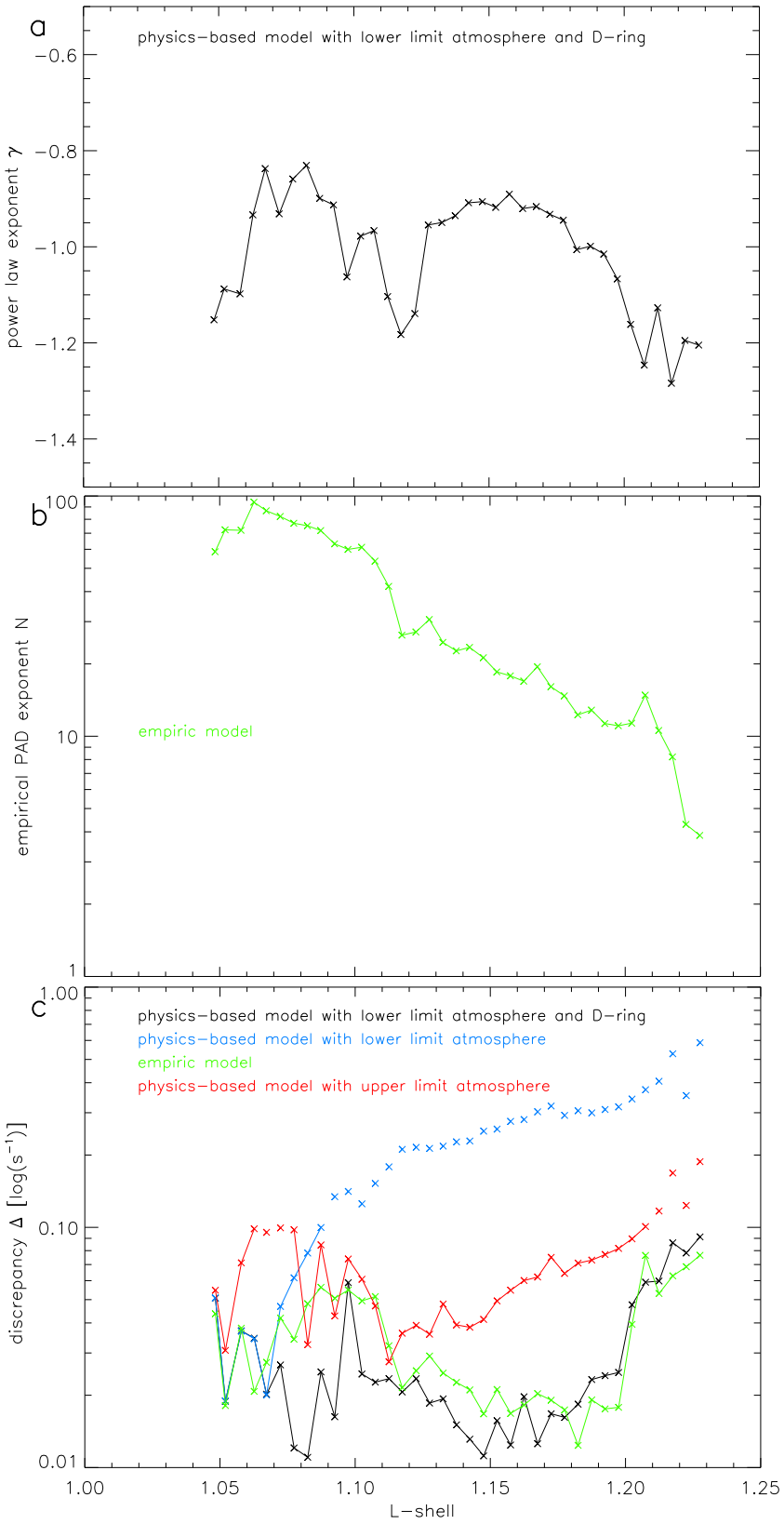

Figure S .1.11. Panel A: Power law exponent γ (Eq. 1) as a function of L-shell. γ shows slight drops where also the overall intensity drops (Fig. 2). Panel B: Exponent N of the empirical PAD (Eq. 4). N decreases when moving from the atmosphere into the D-ring. Panel C: Discrepancy Δ between modeled and measured count rates for different L-shell locations and forward models. $\Delta = 1$ would mean that the average error is 1 order of magnitude. We require $\Delta \leq 0.1$ to consider a result as valid. Only valid points are connected by lines in this panel. It can be seen that the "lower limit" atmosphere model requires combination with the D-ring to yield valid results. Δ assuming the "upper limit" atmosphere is generally higher than the other models, indicating a poor, even though formally valid fit.

References

Berger, M. J., J. S. Coursey, M. A. Zucker, and J. Chang (2005), Stopping-Power and Range Tables for Electrons, Protons, and Helium Ions, The National Institute of Standards and Technology (NIST), http://www.nist.gov/physlab/data/star.

Blake, J. B., H. H. Hilton, and S. H. Margolis (1983), On the injection of cosmic ray secondaries into the inner Saturnian magnetosphere. I - Protons from the CRAND process, *J. Geophys. Res.*, *88*, 803–807, doi:10.1029/JA088iA02p00803.

Cao, H., C. T. Russell, U. R. Christensen, M. K. Dougherty, and M. E. Burton (2011), Saturn's very axisymmetric magnetic field: No detectable secular variation or tilt, *Earth and Planetary Science Letters*, *304*, 22–28, doi:10.1016/j.epsl.2011.02.035.

Cooper, J. F., R. E. Johnson, P. Kollmann, E. Roussos, and E. C. Sittler (2018), *Plasma, Neutral Atmosphere, and Energetic Radiation Environments of Planetary Rings*, p. 363â"398, Cambridge Planetary Science, Cambridge University Press, doi:10.1017/9781316286791.014.

Janni, J. F. (1982), Proton Range-Energy Tables, 1 keV-10 GeV, Energy Loss, Range, Path Length, Time-of-Flight, Straggling, Multiple Scattering, and Nuclear Interaction Probability. Part II. For 92 Elements, *Atomic Data and Nuclear Data Tables*, *27*, 341, doi:10.1016/0092-640X(82)90005-5.

Kollmann, P., E. Roussos, C. Paranicas, N. Krupp, and D. K. Haggerty (2013), Processes forming and sustaining Saturn's proton radiation belts, *Icarus*, *222*, 323–341, doi:10.1016/j.icarus.2012.10.033.

Kollmann, P., E. Roussos, A. Kotova, J. F. Cooper, D. G. Mitchell, N. Krupp, and C. Paranicas (2015), MeV proton flux predictions near Saturn's D ring, *J. Geophys. Res.*, *120*, 8586–8602, doi:10.1002/2015JA021621.

Krimigis, S. M., D. G. Mitchell, D. C. Hamilton, S. Livi, J. Dandouras, S. Jaskulek, T. P. Armstrong, J. D. Boldt, A. F. Cheng, G. Gloeckler, J. R. Hayes, K. C. Hsieh, W.-H. Ip, E. P. Keath, E. Kirsch, N. Krupp, L. J. Lanzerotti, R. Lundgren, B. H. Mauk, R. W. McEntire, E. C. Roelof, C. E. Schlemm, B. E. Tossman, B. Wilken, and D. J. Williams (2004), Magnetosphere Imaging Instrument (MIMI) on the Cassini Mission to Saturn/Titan, *Space Sci. Rev.*, *114*, 233–329, doi:10.1007/s11214-004-1410-8.

Krupp, N., E. Roussos, A. Lagg, J. Woch, A. L. Müller, S. M. Krimigis, D. G. Mitchell, E. C. Roelof, C. Paranicas, J. Carbary, G. H. Jones, D. C. Hamilton, S. Livi, T. P. Armstrong, M. K. Dougherty, and N. Sergis (2009), Energetic particles in Saturn's magnetosphere during the Cassini nominal mission (July 2004-July 2008), *Planet. Space Sci.*, *57*, 1754–1768, doi:10.1016/j.pss.2009.06.010.

Li, W., B. Ni, R. M. Thorne, J. Bortnik, J. C. Green, C. A. Kletzing, W. S. Kurth, and G. B. Hospodarsky (2013), Constructing the global distribution of chorus wave intensity using measurements of electrons by the poes satellites and waves by the van allen probes, *Geophys. Res. Lett.* , *40*(17), 4526–4532, doi:10.1002/grl.50920.

Lindsay, B. G., and R. F. Stebbings (2005), Charge transfer cross sections for energetic neutral atom data analysis, *J. Geophys. Res.*, *110*(A9), A12213, doi:10.1029/2005JA011298.

Mauk, B. H., S. M. Krimigis, D. G. Mitchell, E. C. Roelof, E. P. Keath, and J. Dandouras (1998), Imaging Saturns dust rings using energetic neutral atoms, *Planet. Space Sci.*, *46*, 1349–1362, doi:10.1016/S0032-0633(97)00201-8.

Roussos, E., P. Krupp, C. P. Paranicas, P. Kollmann, D. G. Mitchell, S. M. Krimigis, B. Palmaerts, K. Dialynas, and C. M. Jackman (2018a), Heliospheric conditions at Saturn during Cassini's Ring-Grazing and Proximal Orbits, *Geophys. Res. Lett.* , *this issue*.

Roussos, E., P. Kollmann, N. Krupp, C. P. Paranicas, K. Dialynas, G. H. Jones, D. G. Mitchell, S. M. Krimigis, and J. F. Cooper (2018b), Sources, sinks and transport of energetic electrons near Saturn's main rings, *Geophys. Res. Lett.* , *this issue*.

Roussos and Kollmann et al. (2018), Relativistic protons trapped between Saturn and its rings, *Science*, *under review*.

Schulz, M., and L. J. Lanzerotti (1974), Particle Diffusion in the Radiation Belts, in *Physics and Chemistry in Space 7*, edited by J. G. Roederer, 1st ed., Springer Verlag, Heidelberg, Germany.

Vandegriff, J., R. DiFabio, D. Hamilton, M. Kusterer, J. Manweiler, D. Mitchell, C. Paranicas, and E. Roussos (2013), Cassini/MIMI Instrument Data User Guide, NASA's planetary data system, http://pds-atmospheres.nmsu.edu/data_and_services/atmospheres_data/Cassini/mimi.html.

Walt, M. (1994), *Introduction to geomagnetically trapped radiation*, 1st ed., Cambridge University Press, Cambridge, United Kingdom.